Title: Glacier facies of Vestfonna (Svalbard) based on SAR images and GPR measurements

Author: Barbara Barzycka, Małgorzata Błaszczyk, Mariusz Grabiec, Jacek Jania

Citation style: Barzycka Barbara, Błaszczyk Małgorzata, Grabiec Mariusz, Jania Jacek. (2019). Glacier facies of Vestfonna (Svalbard) based on SAR images and GPR measurements. "Remote Sensing of Environment" (Vol. 221 (2019), s. 373-385), doi 10.1016/j.rse.2018.11.020
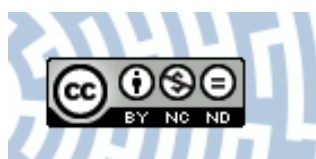
UNIWERSYTET ŚLĄSKI W KATOWICACH   Biblioteka Uniwersytetu Śląskiego   Ministerstwo Nauki i Szkolnictwa Wyższego

Glacier facies of Vestfonna (Svalbard) based on SAR images and GPR measurements

Barbara Barzycka*, Małgorzata Błaszczyk, Mariusz Grabiec, Jacek Jania

University of Silesia in Katowice, Faculty of Earth Sciences, ul. Bedzinska 60, 41-200 Sosnowiec, Poland

ABSTRACT

The warming climate of the Arctic affects the mass budget of glaciers, and changes in the distribution of glacier facies are indicative of their response to climate change. The glacial mass budget over large land ice masses can be estimated by remote sensing techniques, but selecting an efficient remote sensing method for recognizing and mapping glacier facies in the Arctic remains a challenge. In this study, we compared several methods of distinguishing the facies of the Vestfonna ice cap, Svalbard, based upon Synthetic Aperture Radar (SAR) images and terrestrial high frequency Ground Penetrating Radar (GPR) measurements. Glacier zones as determined using the backscattering coefficient (sigma0) of SAR images were compared against GPR data, and an alternative application of Internal Reflection Energy (IRE) calculated from terrestrial GPR data was also used for differentiating the extent of glacier facies. The IRE coefficient was found to offer a suitable method for distinguishing glacier zones and for validating SAR analysis. Furthermore, results of analysis of fully polarimetric Phased Array type L-band Synthetic Aperture Radar (ALOS PALSAR) and European Remote Sensing Synthetic Aperture Radar (ERS-2 SAR) images were compared with the IRE coefficient classification. Especially promising method is H-α segmentation, where the glacier zone boundaries corresponded very well with both GPR visual interpretation and IRE classification results. The IRE coefficient's simplicity of calculation makes it a good alternative to the subjective GPR visual interpretation method, where results strongly depend on the operator's level of experience. We therefore recommend for GPR profiles to be used for additional validation of SAR image analysis in studies of glacier facies on the High Arctic ice masses.

1. Introduction

Global environmental changes have become especially manifest in the Arctic in recent decades. Climate warming influences all parts of the cryosphere, including land ice masses. Glacier mass balance (i.e. glacier mass change over defined timespan – Cogley et al., 2011) therefore serves as an indicator of climate change, although its monitoring is difficult at high latitude, making remote sensing methods important. The Equilibrium Line Altitude (ELA) and glacier facies can be recognized and their spatial distribution mapped using satellite images in visible bands as well as using Synthetic Aperture Radar (SAR) techniques (König et al., 2001a). Therefore, monitoring of glacier zones with remote sensing can be a good indicator of glacier evolution under the influence of climate change.

SAR data offer a particularly suitable method for detecting the extent of glacier facies. Unlike optical satellite imaging, SAR data can also be obtained during polar nights or even in bad weather conditions, as sensors of SAR satellites operate in microwaves range of the electromagnetic spectrum. That makes SAR data independent of sunlight and allows for clouds penetration (Massom and Lubin, 2006). Furthermore, archive SAR data can provide us with feedback regarding climate-glacier interactions in the past.

By analysing the spatial distribution of glacier zones it is also possible to estimate a glacier's mass balance, as an indicator of its current state (König et al., 2004; Jaenicke et al., 2006; Braun et al., 2007). This is especially important because long-term traditional mass balance data have been obtained only for a few dozen reference glaciers (Zemp et al., 2009); thus there is no information on the influence of climate change on larger areas. The exception is the geodetic mass balance, but this method is used mostly for multiyear analyses of changes in the mass of glaciers (Cogley, 2009; Zemp et al., 2009; Nuth et al., 2010). Due to the high availability of SAR data for polar regions, the approximation of mass balance based on the extents of glacier facies may offer a good alternative or complement to geodetic mass balance methods. Nevertheless, selecting an efficient remote sensing method for recognizing and mapping glacier facies in the Arctic still remains a challenge.

---

* Corresponding author.
E-mail address: bbarzycka@us.edu.pl (B. Barzycka).

While glacier zones (facies) were first distinguished by Benson (1961), the best known study on glacier facies was done by Müller (1962), who defined 6 facies: dry snow, percolation A, percolation B, slush, superimposed ice and ice zone. The zones differ in terms of their density and percolation properties (Benson, 1961; Müller, 1962). Based on information about the spatial distribution of glacier facies, Müller (1962) was able to assess the mass balance of the White Glacier, Queen Elizabeth Islands, Canada. Nowadays, with advanced SAR satellite sensors, it is possible to provide mass balance information for most regions, even inaccessible ones. In our study, as in other studies of glacier facies on Svalbard (e.g. Engeset et al., 2002; König et al., 2004; Brandt et al., 2008; Akbari et al., 2014), three main zones were distinguished, typical for this area: ice, superimposed ice and firn. The firn zone was divided into two smaller zones: firn < 4.5 m and firn > 4.5 m of thickness, which may correspond to percolation zone B and A defined by Müller (1962). An additional class, defined as 'ice+', was distinguished as well. Ice+ is characterised by a clear, unique GPR backscatter, which is nevertheless difficult to identify as a one of the well-known glacier facies.

Determination of the superimposed ice (SI) zone is still problematic in mass balance analysis performed using remote sensing methods. SI belongs to the accumulation zone and can be found between firn (accumulation zone) and glacier ice (ablation zones). The main difference between glacier ice and SI is that the former is created by the metamorphism of snow in the accumulation zone of the glacier, while SI is created by refreezing of melted water from the upper part of the glacier or rain freezing on contact with ice (Baird, 1952; Obleitner and Lehning, 2004). Thus, the lower boundary of SI zone can determine location of ELA. The similar physical properties of SI and glacier ice, however, may cause their misinterpretation, leading to misestimation of the accumulation component of the glacier as SI can be an important element in mass balance assessments (Wakahama et al., 1976; Wright et al., 2005). Because of this similarity, in analysis of optical imagery it is very difficult or even impossible to distinguish the SI zone and the equilibrium line, the most important indicator of a glacier's state. This limitation seems not to apply to SAR data, as microwaves are, for instance, sensitive to air bubble content, which is relatively high in SI (König et al., 2002). However, the ability to distinguish the SI zone on SAR images is still open to question. Several studies (König et al., 2002; Langley et al., 2008; Brandt et al., 2008; Akbari et al., 2014) show that the SI zone detected on SAR data is in good agreement with field measurements. However, all such successful comparisons of SAR and ground-truth data concern only the Kongsvegen glacier (Svalbard) in the years 1999, 2000 (König et al., 2002), 2003 (Brandt et al., 2008) and 2008 (Langley et al., 2008; Akbari et al., 2014). A study of the very same glacier by (Engeset et al., 2002) for the years 1991–1997 on the other hand, reported an inability to distinguish the SI zone by backscattering coefficient analysis. Also, König et al. (2002) provided promising results of SI detection for Kongsvegen but not for Midre Lovénbreen, reporting at the same time an inability to discriminate between summer and winter formed SI for both glaciers. Finally, Casey and Kelly (2010) reported uncertainty in distinguishing the SI zone on SAR images for the Devon Ice Cap, Canada. Details of SAR data used in the mentioned studies are presented in Table 1. In this paper, we once again address the question on the possibility of distinguishing the SI zone by means of remote sensing.

Not only the SI zone in particular, but all types of glacier facies have been distinguished using SAR data for many years (e.g. Rott and Nagler, 1993; König et al., 2004; Huang et al., 2013). However, the precision of their delineation is very often problematic. Only some of the relevant projects involve comparison to ground-truth data. If they do, the Ground Penetrating Radar (GPR) profile, in which an experienced operator can distinguish glacier zones, is usually used to validate the SAR analysis (Engeset et al., 2002; Langley et al., 2008; Doulgeris et al., 2009; Akbari et al., 2014). However, this method of validation can be affected by subjective interpretation or a lack of experience on the part

of the operator; moreover, the difficulty of visual interpretation of the GPR profile makes it time-consuming. Therefore, we resolved to explore the possibility of using the Internal Reflection Energy (IRE) coefficient to differentiate glacier facies on GPR data. Application of the IRE coefficient can be expected to reduce both the impact of subjectivism in the research and time required for analysis of GPR measurements. Analysis of glacier facies by means of IRE coefficient is therefore simplified, objective and performable by someone inexperienced in GPR visual interpretation.

The information about extents of glacier facies is especially important after the end of ablation season. This time is significant for glaciers monitoring as glacier facies extents are in their extrema, the ELA in its annual maximum and the glacier's mass is in its annual minimum (Benn and Evans, 2010). By comparison of those measures in annual scale it is possible to describe glacier's state and its response to climate changes. However, the time of the end of the ablation season differs from glacier to glacier (due to e.g. latitude or local climate) and from year to year (depending on e.g. temperature and precipitation). This considerable limits abilities of recognition of glaciers zones at that time. Nevertheless, the extents of glacier facies in their extrema can be observed during following accumulation season, when the temperatures below 0 °C dominate. This is due to the preservation of glacier facies in negative temperatures, high penetration of dry snow by SAR waves and the best efficiency of GPR under dry snow conditions. The main limitation of the distinguishing glacier facies during the accumulation season could be a presence of water in the snowpack (after e.g. rain-on-snow event or mid-winter thaw) which reduces the penetration of the snowpack by SAR (Rott and Nagler, 1993; Marshall et al. 1995 as cited in Brown et al., 1999) and strongly attenuates GPR waves (Melvold, 2008; Gusmeroli et al., 2014). Also a high amount of ice layers in the snowpack may affect the efficiency of described methods (Mätzler and Schanda 1984 as cited in Hall et al., 2005, Hall et al., 2005, Kanagaratnam et al., 2004).

The present study is a next step in distinguishing glacier facies by robust methods in the future. We examined several methods of distinguishing glacier facies, including analysis of the terrestrial GPR data by visual interpretation and the IRE classification method. Further, backscattering coefficient (sigma0) classification of satellite SAR data (European Remote Sensing Synthetic Aperture Radar – ERS-2 SAR and Phased Array type L-band Synthetic Aperture Radar – ALOS PALSAR) was carried out. Finally, the results of distinguishing glacier facies by IRE coefficient classification, results of k-means classification and polarimetric analysis (Pauli decomposition and H-α segmentation) were compared. Note that both L-band sigma0 analysis and scattering decomposition and segmentation of fully polarimetric SAR images with validation by in situ data, has virtually not been applied to glacier facies detection before. The exception being a study by Doulgeris et al. (2009), but their results of the GPR visual interpretation were much less detailed than those of SAR decompositions, making validation impossible. Błaszczyk (2012) presented very good results of glacier facies detection by remote sensing methods based on ERS-2 SAR and ALOS PALSAR images and visual validation of results with GPR data. The present study further develops and improves this new approach to fully polarimetric image decomposition application, using Vestfonna data as an example.

2. Study area

The presented data focus on the Vestfonna ice cap, located in the north-west part of Nordaustlandet, an island in the Svalbard archipelago (Fig. 1). Vestfonna is Svalbard's second largest ice cap, covering over 2400 km^2 (Nuth et al., 2010). The altitude of this polythermal ice field varies from 0 to 630 m above sea level (asl). The geodetic total mass balance of Vestfonna was estimated as close to 0 m/yr for 1990–2007 (Nuth et al., 2010), with the annual mean equilibrium line altitude (ELA) of the ice cap at 383 ± 54 m asl (Möller et al., 2011a).

Table 1
Details of SAR data used in the prior studies of SI detection with comparison to in situ data. Acronyms used in the table: European Remote-Sensing Satellite-1 (ERS-1), European Remote-Sensing Satellite-2 (ERS-2).

Article	Year(s) of SAR acquisition, location	SAR data source	SAR frequency	SAR polarisation	Comments
König et al. (2002)	1999, 2000	ERS-1	5.3 GHz (C-band)	VV	SI detected on Kongsvegen, difficulties on Midre
	Kongsvegen, Midre Lovénbreen	ERS-2	5.3 GHz (C-band)	VV	Lovénbreen
	(Svalbard)	RADARSAT-1	5.3 GHz (C-band)	HH	
Engeset et al. (2002)	1991–1997 Kongsvegen (Svalbard)	ERS-1	5.3 GHz (C-band)	VV	Difficulties in SI detection
		ERS-2	5.3 GHz (C-band)	VV	
Langley et al. (2008)	2005	ENVISAT ASAR	5.3 GHz (C-band)	HH, VV,	SI detected
	Kongsvegen (Svalbard)			HV, VH	
Brandt et al. (2008)	2003	ERS-2	5.3 GHz (C-band)	VV	SI detected
	Kongsvegen (Svalbard)				
Casey and Kelly (2010)	2004–2006	RADARSAT-1	5.3 GHz (C-band)	HH	SI not detected
	Devon Ice Cap (Canada)				
Akbari et al. (2014)	2005	ENVISAT ASAR	5.3 GHz (C-band)	VV/VH, HH/HV	SI detected
	Kongsvegen (Svalbard)				

The snowpack of Vestfonna is characterised by homogenous density and low interannual and spatial variability (Möller et al., 2011b). The monthly average temperatures for Vestfonna range from −15 to –10 °C in winter and do not exceed +3 °C in summer months (Möller et al., 2011a). Despite Vestfonna's high latitude, short events of temperatures significantly higher than the monthly average values do occur (Möller et al., 2011a) due to its maritime climate and due to global changes. However, based on meteorological data (Möller et al., 2011a), no such event occurred within the time frame of this study.

3. Data

3.1. Synthetic Aperture Radar (SAR)

In this study, both ERS-2 SAR and ALOS PALSAR products were analysed (Table 2). The former sensor operated in C-band with a frequency of 5.3 GHz, the latter in L-band with a frequency of 1270 MHz. L-band ALOS PALSAR images are characterised by longer wavelengths

(∼23.5 cm) than ERS-2 SAR (5.7 cm). ALOS PALSAR measured amplitude and phase in all polarisations (HH, HV, VH, VV), enhancing the detection and monitoring capabilities of glacier facies, as the polarimetric phase contains more information on structural characteristics of the scatterer. Cross-polarisation (VH or HV) gives information based largely on volume scattering, whereas co-polarised signals (HH or VV) are largely contributions from surface scattering (Massom and Lubin, 2006). To reduce the randomness of the results of analysis based only on one image (due to e.g. high speckle noise or differences in acquisition geometry), we analysed all ERS-2 SAR images acquired in May 2009 which fully cover the area of interest (Table 2).

All data were provided in the form of Single Look Complex (SLC) products, and only minimum number of corrections were applied. Based on an algorithm provided by Laur et al. (2004) all ERS-2 SAR images were fully calibrated by application of: Analogue to Digital Convertor (ADC) power loss correction, removing replica pulse power, incidence angle correction, calibration constant, antenna elevation pattern gain and range spreading loss correction. In the next step the
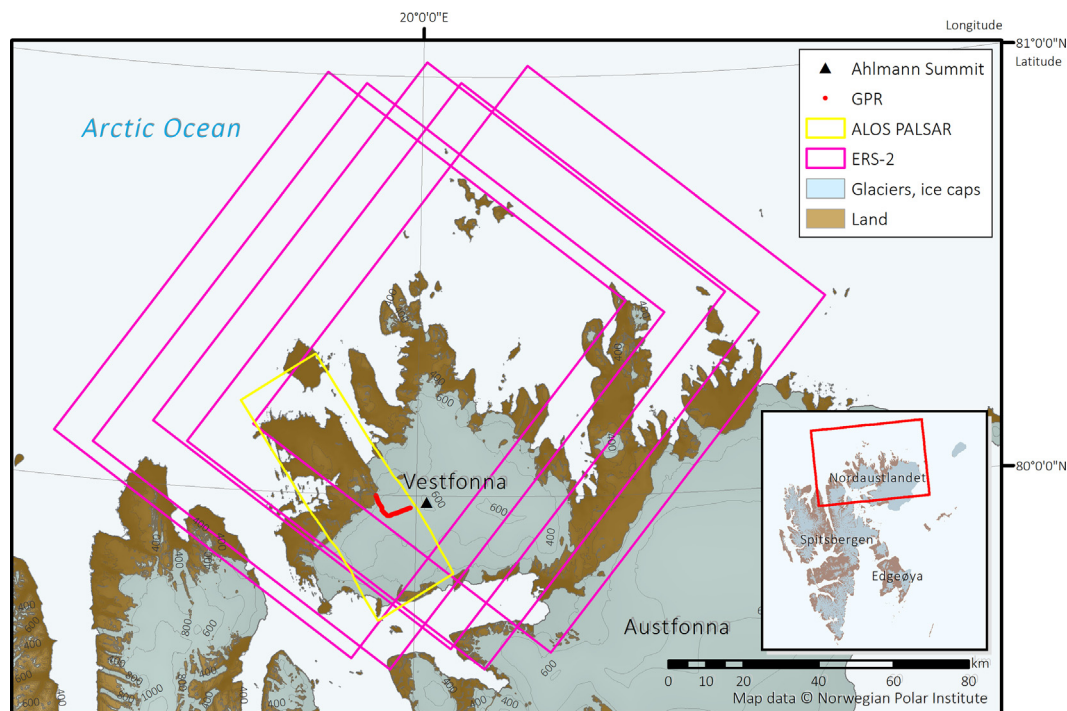

Fig. 1. Study area, showing the extent of ALOS PALSAR (yellow), the extent of ERS-2 SAR (purple) and the track of GPR measurements (red). Black triangle marks the location of Ahlmann Summit and the red box on the overview map in the lower right corner the extent of the main map of the Figure above. Basemaps provided by the Norwegian Polar Institute (npolar.no). (For interpretation of the references to colour in this figure legend, the reader is referred to the web version of this article.)

Table 2
SAR data used in the project with information about sensor, acquisition date, polarisation, reference incidence angle, orbit number and pass.

Sensor	Acquisition date	Polarisation	Incidence angle	Orbit	Pass
ERS-2 SAR	04.05.2009	VV	23°	73395	Descending
	07.05.2009	VV	23°	73438	Descending
	20.05.2009	VV	23°	73624	Descending
	23.05.2009	VV	23°	73667	Descending
	26.05.2009	VV	23°	73710	Descending
ALOS PALSAR	22.05.2009	VV, HH, VH, HV	25.706°	17719	Ascending

images were geometrically corrected and geocoded by applying Range-Doppler Terrain Correction algorithm (Small and Schubert, 2008). The images were resampled into the geographical location of the image acquired on 20 May 2009. The final geolocation of all ERS-2 SAR products was checked based on terrain features and coastline with comparison to Landsat 7 images. Finally, following successful study of Langley et al. (2008) all ERS-2 SAR data were averaged into one image with pixel spacing of 12.5 m. Neither multilooking nor speckle filtering processes were applied at this stage as the applied averaging of the images reduced most of the speckle.

ALOS PALSAR SLC 1.1 level products are characterised by non-zero-Doppler times annotations so the geometry of the data is distorted. Therefore, the image was a subject of deskewing process in order to transform the image into a zero Doppler like geometry. For radiometric calibration an absolute calibration constant was applied (Lavalle and Wright, 2009). The speckle effect was reduced by a Lee Speckle Filter (5 × 5 window size). For geometric correction and geolocation of the final product (21.5 m pixel spacing) Range-Doppler Terrain Correction algorithm was used.

3.2. Ground Penetrating Radar (GPR)

The shallow ground-based radio-echo soundings used for the validation of SAR data were carried out on Vestfonna in 18 May 2009 (Grabiec et al., 2011; Sauter et al., 2013). The GPR set, equipped with an 800-MHz shielded antenna, was pulled on a sledge behind a snowmobile. A total of 90 km of profiles were investigated on both the ice cap slopes and the upper part of the dome. Measurements were positioned using a dual-frequency GPS receiver fixed on the snowmobile. GPS positions obtained by the rover were processed based on data from the reference GPS module working simultaneously at a fixed point in the Vestfonna forefield. Positions were collected at intervals of 1 s, whereas the GPR signal was collected every 0.5 s. Taking into account the trace interval and the mean movement speed of the GPR set, every trace was attributed to an average distance of 2.1 m. The GPR trace consists of 710 samples in a 70.2-ns time window, which – with regard to the radio wave velocity in the materials forming the surficial ice cap layer – enables penetration of the snow cover as well as the underlying structures of glacier ice, superimposed ice, or firn down to 6.9 m. The processing of GPR data, as a preparatory phase to IRE calculation, includes a DC-removing filter only. This enables maximal preservation of the original signal.

4. Methods

4.1. Visual interpretation of GPR

Over 12 km of total 90 km of GPR profiles obtained along the ice cap was interpreted visually for further validation of SAR and IRE classification. The chosen profile (Fig. 1) starts at the terminus of the ice cap, reaching central ridge and ending close to Ahlmann Summit (622 m n.p.m.) on the top of the ice cap, ensuring that all glaciers facies were crossed by the GPR track. After appropriate processing, the GPR profile was examined to define sub-snow characteristics within the specified time window. The basis for the analysis consisted of the location of the

individual section of the profile and the GPR image structure, as properly interpreted by an experienced operator. Five zones were distinguished. In the lowest part of the ice cap the 'ice' zone was identified. In this section, a highly homogenous structure was noted, without layering and with limited diffractions, characteristics typical of glacier ice. Next, the 'ice+' zone was distinguished, where a thin layer of undefined properties was located between the glacier ice and the snow. Probably this stratum is of accumulation origin or forms a very rough ice surface filled by the snowpack. The ice+ layer is transformed into the following zone, characterised by thicker, unstratified structure derived from secondary accumulation, hereinafter referred to as "SI". However, due to lack of ground-truth validation data from this zone, it cannot be ruled out that this form may be superimposed ice or thin firn from previous seasons. Up-glacier, stratified structures were noted underneath the snow cover, increasing in number and thickness towards the top of the ice cap. This pattern is typical for firn layers. This zone was divided into 2 parts depending on the depth of the firn sole: 'firn < 4.5 m' and 'firn > 4.5 m', respectively.

4.2. Internal Reflection Energy (IRE)

Gades et al. (2000) defined Internal Reflection Power (IRP) as the mean value of the amount of reflected energy for the sample in each trace within a defined time window of GPR measurements. IRP is calculated as one-half of the sum of the squared amplitudes divided by the number of samples in the time window. This index was modified by Jania et al. (2005) in a study of temporal changes in the radiophysical properties of Hansbreen (Svalbard), where IRP was not suitable because of the strong variations in glacier layers along the GPR profile occurring in polythermal glaciers. Accordingly, Jania et al. (2005) decided to use a variable-width time window and calculate Internal Reflection Energy (IRE) using the IRP equation without dividing by the number of samples in the time window. Thanks to this modification, it is possible to receive information about total reflected energy, instead of the average power calculated by IRP.

Although both IRP and IRE have been applied mostly to investigations of ice and bedrock properties and water presence (Gades et al., 2000; Jania et al., 2005; Navarro et al., 2005), IRE was adopted by Grabiec (2017) to distinguish glacier facies on Hansbreen (Svalbard). In our study IRE was calculated only for a GPR time window from 20 to 70 ns, i.e. a period during which all layers should be registered, except for dry snow. In May 2009 snowpack depth in the studied area ranged between 0 m (on wind erosion areas) and 2.24 m, with an average thickness 1.12 m (Grabiec et al., 2011). Snow pits in the accumulation area revealed an absence of ice lenses in the snowpack (Möller et al., 2011b). Applying the mentioned time window, IRE should represent similar volume as SAR data, where dry snow is penetrated by microwaves, thus is invisible on the images. The exception is snowpack with ice layers after rain-on-snow or thaw events or snow grain size at least as large as the SAR wavelength (Mätzler and Schanda 1984 as cited in Hall et al., 2005, Hall et al., 2005), what may contribute to the total value of sigma0 and influence further classification. In this study however it should not be the case as both C- and L-band wavelengths are larger than the grain size and Vestfonna's snowpack is characterised by lack or low amount of ice lenses (Möller et al., 2011b).

In addition, noise power (NP) for all investigated traces was calculated using the IRP formula with a time window of 2 ns prior to recording of the direct wave. This was done in order to estimate the background noise (Jania et al., 2005) caused mainly by the GPR set. IRE values were averaged in each pixel of the ALOS PALSAR image based on the geolocation of each sample.

The IRE values were presented in the form of a scatter plot and a boxplot. For the purposes of the boxplot, each IRE value was assigned to one of the classes (ice, ice +, SI, firn < 4.5 m, firn > 4.5 m) according to visual interpretation results. This allowed the distribution of IRE values to be analysed in each class.

4.3. Backscattering coefficient (sigma0) of SAR data

The main parameter related to SAR techniques is the backscattering coefficient (sigma0). This factor represents the quantity corresponding to microwave reflectance from the scatterers in each resolution cell recorded by the sensor (Rees, 2005). The value of the backscattering coefficient depends more on physical than chemical properties (Ferretti et al., 2007); thus, SAR data can be used effectively to distinguish glacier facies. Among the factors influencing backscattering, two groups can be distinguished: scattering characteristics and satellite parameters. The former depend, for instance, on the roughness and geometry of the scatterer and its dielectric properties, the latter for instance on the polarisation, wavelength, and incidence angle of the microwave (Rott and Mätzler, 1987; Lillesand et al., 2008). An especially important role in analysing the extent of glacier facies is played by the dielectric properties of the volume and hence the presence of liquid water. Several studies (e.g. Rott and Nagler, 1993; Marshall et al. 1995 as cited in Brown et al., 1999) have revealed that even a small amount of liquid water (~3–5% of liquid water content) in a snow layer can dramatically affect penetration of the layer by microwaves. Thus, in order to distinguish glacier zones, it is necessary to analyse only imagery obtained during winter or early spring, when the absence of liquid water enables analysis of backscattering of volume, not of a surface (König et al., 2001a). As opposed to remote sensing techniques operating in the optical spectrum, the presence of dry snow cover during winter is not problematic due to the high degree of penetration of this layer by microwaves, which is related to the absence of water and small grain size (Hall, 1996; Rees, 2005).

Backscattering value analysis is commonly used in distinguishing glacier facies (e.g. Partington, 1998; Langley et al., 2008) as sigma0 varies along glaciers profiles. Upper parts of glaciers with a lack of dry-snow zone, are characterised by high backscattering values due to volume scattering typical for firn areas or presence of ice lenses (Fahnestock et al., 1993). In the contrary, low values of sigma0 represent the ablation area, were SAR signal is reflected from glacier ice, which acts as a specular reflector (König et al., 2000). However, among the low backscattering values of glacier ice, high sigma0 can occur due to presence of crevasses resulting in strong reflection of the signal. Moreover, backscattering coefficient values can be influenced by a character not only of a surface but also a subsurface of a glacier. This highly depends on the wavelength of the SAR sensor. The dependence was described in the study of König et al. (2001b) where airborne L-band microwave revealed crevasses in the accumulation area, invisible for a shorter C-band airborne sensor. Another study (Rignot et al., 2001) shows, that airborne C-band can penetrate 1–2 m on bare ice and up to 10 m in dry firn, whereas penetration of airborne L-band is ~5–10 m greater, influencing the final value of the backscatter. The property of L-band penetration was applied in a research of Alpine glaciers based on airborne three-dimensional SAR tomography method (Tebaldini et al., 2016) where the scattering patterns of L-band in different areas of the glacier was described. Analysis of SAR data and in situ data measurements revealed that the scattering of L-band is dominated mainly by subsurface scattering with a contribution from volume scattering of firn, crevasses or even bedrock. The domination of

L-band subsurface scattering and pervious applications of C-band imageries (see Table 1) imply that both wavelengths should be suitable for distinguishing glaciers facies.

Based on the encouraging results of the aforementioned studies, in this research sigma0 values are extracted from both ALOS and averaged ERS-2 images along the GPR profile (Fig. 1) and compared to GPR measurements represented by the IRE coefficient. Since HH/VV and HV/VH polarisation modes yield similar results (Massom and Lubin, 2006), only sigma0 values extracted from VV and VH imaging were analysed. As in case of IRE, boxplots for sigma0 values for each of the images were done, presenting the distribution of the coefficient in each class.

4.4. Natural breaks (Jenks) classification

Both sigma0 and IRE values were also classified into 5 classes using the natural breaks (Jenks) method. The natural breaks classification groups values of a dataset into classes in order to achieve the lowest variations within the each class and – at the same time – the highest variations between the classes (Jenks and Caspall, 1971; De Smith et al., 2007). The results of the classification are presented in the form of maps.

4.5. Polarimetry and SAR image classification

In addition to simple analysis of backscatter coefficient values of SAR data, scattering decomposition is widely applied to the interpretation, classification, and segmentation of SAR polarimetric images (Cloude and Pottier, 1996; Lee et al., 1999). However, fully polarimetric data and their decomposition are still not commonly used in glaciology. Singh et al. (2010, 2014) studied the capability of fully polarimetric L-band data concerning snow and non-snow areas whereas Venkataraman et al. (2007) discussed the capability of fully polarimetric L-band ALOS PALSAR data for snow classification. Brown (2013) focused on changes in backscatter over time by polarimetric decomposition studies. Huang et al. (2011) analysed fully polarimetric SAR images obtained in August, thus the high water content in the snowpack allowed only ice and wet snow zones to be detected. The only study of glacial zone discrimination on Svalbard using fully polarimetric L-band SAR image with validation by GPR visual interpretation was made for Vestfonna (Błaszczyk, 2012). Author applied Pauli RGB decomposition and H/α segmentation to ALOS images with the use of the ESA open-source software PolsarPro (López-Martínez et al., 2005). Pauli colour coding is based on a vector representation of linear combinations of scattering matrix elements. Matrix parameters are related to the target itself, i.e. the geometrical structure and dielectrical properties of the object. The resulting polarimetric channels HH + VV, HH-VV, and HV are then associated with the colours blue, red, and green, respectively (López-Martínez et al., 2005). Based on the characteristics of each combination, different types of scattering mechanisms are represented by RGB colours. For example, blue indicates targets characterised by single- or odd-bounce, red double- or even-bounce mechanisms (e.g. built-up areas), green a dominant HV component, generally characteristic of vegetated zones (volume scattering) (López-Martínez et al., 2005).

In polarimetric decomposition H/A/α, three parameters are defined: entropy – H; anisotropy – A; and mean alpha angle – α. A study of the scattering mechanism is performed mainly through the interpretation of the mean alpha angle, whereas entropy H determines the degree of randomness of the scattering process (López-Martínez et al., 2005). Cloude and Pottier (1997) proposed an algorithm to identify, in an unsupervised way, polarimetric scattering mechanisms in the H-α plane. The H-α classification plane is subdivided into 8 basic zones characteristic of different scattering behaviours and one zone of nonfeasible region, where the differentiation of the scattering mechanism is not possible (Cloude and Pottier, 1997; SNAP ESA, 2018).

Segmentation in the H-α plane enables identification of the type of scattering mechanism: surface reflection, volume diffusion, and double bounce reflection along the α axis, and low, medium, and high degrees of randomness along the entropy axis (Cloude and Pottier, 1997, SNAP ESA, 2018). The algorithm was improved by Lee et al. (1999) by implementation of an iteration process of pixels reclassification based on their Wishart distances (Lee et al., 1994) to centres of clusters (H-α Wishart classification). Although Błaszczyk (2012) carried out exclusively visual validation of results with glacier zones determined from GPR visual interpretation, these initial studies show the usefulness of fully polarimetric data in the determination of glacier facies. In this study, we sought to improve upon the interpretation of Pauli RGB decomposition and H/α segmentation of fully polarimetric ALOS PALSAR imaging, as made by Błaszczyk (2012), by adding the objective method of IRE classification.

Additionally, for comparison of results of analysis of fully polarimetric L-band data with C-band data, the averaged ERS-2 SAR images classified with the use of standard pixel unsupervised classification (k-means) was compared to the IRE coefficient classification. In the k-means classification method, classes are created by automatic choice of values of pixels as centres of the classes to which all the other pixels are assigned based on the distance to the closest class centre. After the classification processing of the first iteration the centres of the classes are set anew as values corresponding to centroids of the classes resulting from the previous step. The process is repeated till there is no difference between the iterations or if the maximum number of iterations was reached (MacQueen, 1967). Before the k-means classification, the averaged ERS-2 SAR image was limited to the area covered by all five images and the GPR measurements, to ensure the average value of each pixel was calculated based on the same amount of images. To remove still noticeable speckle noise, Lee Speckle filter (5×5 window size) was applied. This resulted in reduction of speckle noise with preservation of changes in sigma0 values along the distinguished glaciers facies. The number of 16 clusters of the classification was chosen based on elbow method (Thorndike, 1953) and Bayesian information criterion (Schwarz, 1978) which are statistical approaches in determining the number of classes in k-means algorithms.

5. Results

5.1. Visual interpretation of GPR

As a result of the visual interpretation of GPR data, 5 classes were distinguished: ice, ice +, SI, firn < 4.5 m thick (firn < 4.5 m), and firn > 4.5 m thick (firn > 4.5 m) (Fig. 2).

5.2. Internal Reflection Energy

The results of IRE and NP calculations compared to the visual interpretation of GPR are presented in Fig. 3. NP values remained stable for the entire GPR profile, which means that noise was at a constant level throughout the measurements. Thus, it can be assumed that IRE values are consistent, since the noise influenced GPR measurements constantly throughout the profile.

The IRE varied between 45 and 65 dB. There is a distinct difference in variations between classes with the presence of ice, such as ice or ice +, and the remaining classes, in which variations in IRE values are by one order of magnitude higher (Table 3). This is due to the consistent structure of ice facies and their uniformly high density, thus the variations in this zones are low. The increase in value of IRE between ice + and SI facies is shifted in favour of the ice + zone, probably due to the fixed time window of IRE calculation. Because of the simplification of the IRE calculation caused by applying a constant time window through the whole GPR profile, that part of the significant SI volume was not taken into account in the calculation process. As a result, the values of IRE of the lower part of the SI zone are on the same level as ice +. Note

that the choice of the time window was made in order to ensure that the snow cover would not exert an influence on IRE calculation. Another possible reason is subjectivity of the GPR visual interpretation of both ice + and SI classes, which cannot be resolved due to the lack of ground-truth validation data.

Absolute values and variations of IRE for features classified as firn are higher (Table 3, Fig. 3); this is caused by higher spatial variation of density (both horizontally and vertically) and by the character of the scatterers. Ice, on the other hand, with its consistency and significantly lesser amount of air, causes poorer conditions for the reflection of radar waves but greater homogeneity of IRE values.

5.3. Backscattering coefficient (sigma0) of SAR data

Values of sigma0 vary between -23 and 5 dB for ALOS PALSAR VH image, -15 and 6 dB for ALOS PALSAR VV and -13 and 5 dB for averaged ERS-2 SAR data (Fig. 4). The backscattering coefficient values rise throughout the profile, with a difference of ~10 dB between ice in the lowest part of Vestfonna and firn in the most upper part. In addition, sigma0 values extracted from ALOS PALSAR VH are ~10 dB lower throughout the profile than ALOS PALSAR VV. This difference was also reported by König et al. (2001b) and it is related to the physics of surface and subsurface scattering and change of polarisation by the scatterer. The influence of the polarisation is in the good agreement of ALOS PALSAR VV and averaged ERS-2 SAR VV sigma0 values. In addition, standard deviations of ALOS PALSAR VH values are higher by minimum one order of magnitude comparing to standard deviations of analysed co-polarised images (Table 4). Due to high consistency of the internal structure of Vestfonna only small differences between sigma0 of C- and L-band VV images can be observed. Only one marked decline of ALOS PALSAR sigma0 values at the 6.7 km distance from the front of the ice cap indicates a presence of a buried feature or lower value of reflectance from ice under firn which was not penetrated by a shorter wave of ERS-2 SAR. On the other hand, at the distance of 0.4 km of the GPR profile, the averaged ERS-2 SAR sigma0 values increase in the contrary to the ALOS PALSAR sigma0. The difference in the penetration depth of C- and L-band explains also higher values of backscattering coefficient of ALOS PALSAR VV comparing to ERS-2 SAR in firn zones, where volume scattering is dominant thus stronger for longer wavelengths.

Incidence angles of both ERS-2 SAR products and ALOS PALSAR were similar (Table 2), so this parameter should not have a big influence on the differences in sigma0 values. In addition, as all changes in the glaciers facies are along west-east part of the profile and the slope of the ice cap is rather gentle (Fig. 2), the difference between ascending and descending orbits of the SAR satellites also should have a small impact on backscattering coefficient values.

5.4. Sigma0 and IRE comparison

Based on backscatter coefficient values limited to the 1st and 3rd quantiles (top and bottom of a box, Fig. 5, left panel) for the ALOS PALSAR VH, it is possible to differentiate all classes except ice and ice +. In the case of the ALOS PALSAR VV (Fig. 5, left panel) all classes are distinguishable, with a small overlap of the ice + and SI classes. The difference is caused by the character of polarisation: co-polarised waves are better suited for surface roughness, cross-polarised for volume scattering (Massom and Lubin, 2006). Backscatter coefficient values extracted from the averaged ERS-2 SAR image (Fig. 5, central panel) differentiate between each class except SI and firn < 4.5 m. The differences related to the wavelengths of C-band ERS-2 SAR and L-band ALOS PALSAR are visible in the total range of values for classes representing ice and firn facies. As the L-band penetrates deeper, boxes of classes such as SI, firn < 4.5 m, and firn > 4.5 m are wider distributed than for the averaged ERS-2 SAR image and are more easily distinguished. Similarly, backscatter coefficient values for ice, ice +, and
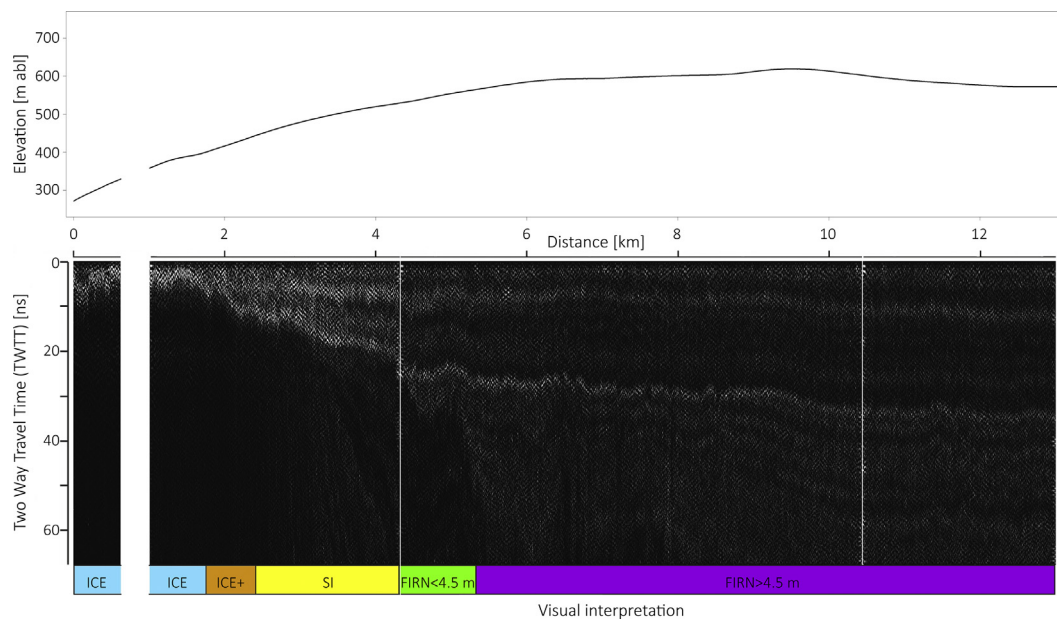
Fig. 2. Results of GPR visual interpretation with elevation profile in the upper panel. Symbols of classes: blue – ice, orange – ice+, yellow – SI, green – firn < 4.5 m, purple – firn > 4.5 m (location of GPR measurements in Fig. 1). (For interpretation of the references to colour in this figure legend, the reader is referred to the web version of this article.)

SI on the ERS-2 SAR image are clearly separated and thus more easily identified.

A boxplot was also generated for IRE values and compared with the boxplots for sigma0 values (Fig. 5, right panel). It can be seen that the boxes for ice and ice+ are on a similar level. This is probably due to the fixed time window selected for IRE calculation, as described above. The classes firn < 4.5 m and firn > 4.5 m are difficult to distinguish. This is caused by the natural continuity of the two classes, the character of whose scatterers are very similar in the total measured volume. The clearly different class of SI visible in the IRE boxplot is very promising for further studies, since the SI zone as far as identified with superimposed ice, though difficult to differentiate, may be very important in mass balance estimation.

5.5. Natural breaks (Jenks) classification of sigma0 and IRE

Both IRE and sigma0 coefficients were divided into 5 classes using the natural breaks method (Fig. 6). Additionally, boundaries between glacier zones obtained from visual interpretation of GPR were marked by red lines in Fig. 6a–e. Although in the case of IRE values (Fig. 6b) the boundaries between such classes as ice and ice+, firn < 4.5 m and firn > 4.5 m are not clear, the SI zone is possible to differentiate, with shifted ice+/SI boundary due to the fixed time window of IRE calculation. This indicates it is possible to distinguish ablation (ice) and accumulation zones (SI and firn), which is important in mass balance assessment.

Both ALOS PALSAR and ERS-2 SAR images yield very promising results. For the cross-polarised ALOS PALSAR image (Fig. 6c), all classes except ice and ice+ can be distinguished via simple classification of sigma0 value. The slightly shifted boundary between firn < 4.5 m and firn > 4.5 m may be caused by the natural continuity of the two facies, resulting in similarity in scattering in volume. In the case of ALOS PALSAR with VV polarisation (Fig. 6d), only ice+ and SI have no clear boundary. The results of the classification of sigma0 values extracted from averaged ERS-2 SAR images (Fig. 6e) show that it is possible to differentiate glacier facies which differ more on the surface (ice, ice+) than on the subsurface level. Although the penetration of the ERS-2 SAR C-band is shallower than of the ALOS PALSAR L-band, due to cold, dry
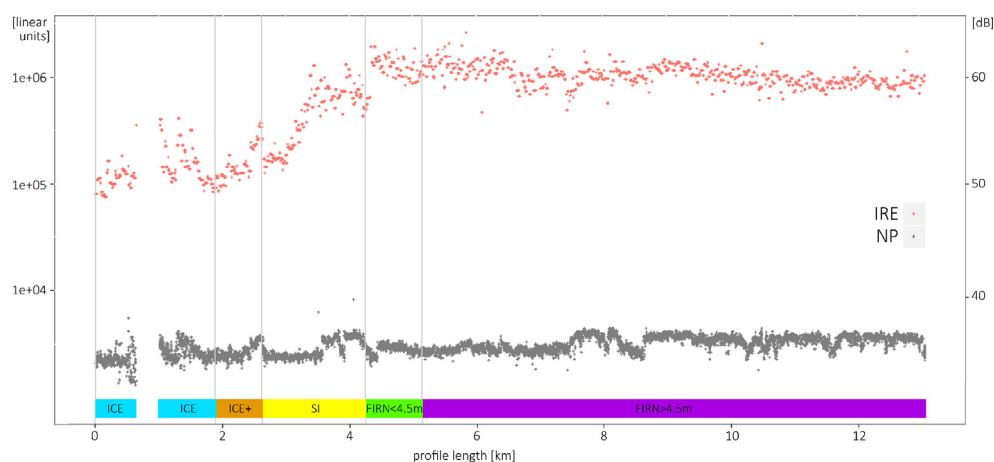

Fig. 3. IRE and NP values compared to visual interpretation of GPR measurements (bottom panel). Left Y axis is presented in linear units (logarithmic scale), right Y axis in decibels.
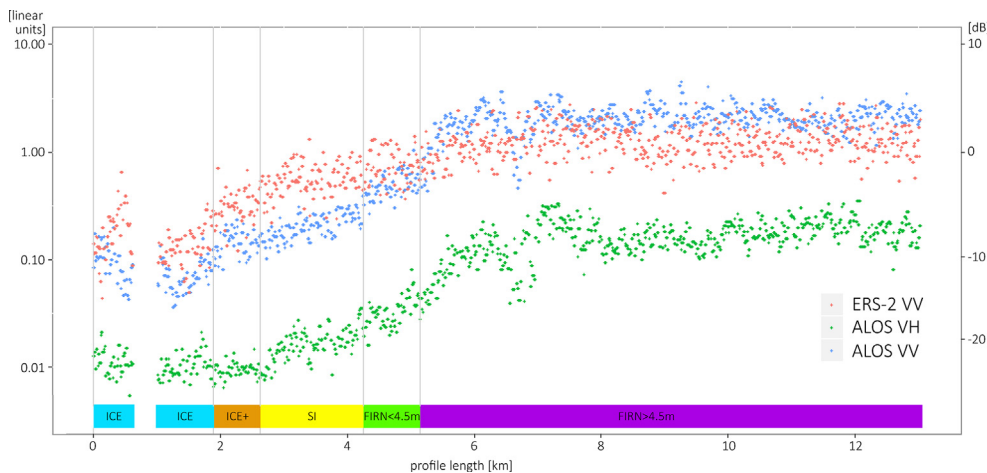
Fig. 4. Backscattering coefficient values along the GPR profile for ALOS PALSAR VH (green), ALOS PALSAR VV (blue) and ERS-2 SAR average product (red). Left Y axis is presented in linear units (logarithmic scale), right Y axis in decibels. (For interpretation of the references to colour in this figure legend, the reader is referred to the web version of this article.)

conditions and snow depth up to 2.24 m along the GPR profile (Grabiec et al., 2011) it was possible to distinguish the firn > 4.5 m class.

5.6. Polarimetric decomposition and k-means classification vs. in situ data

Here we compare Błaszczyk's (2012) results and k-means classification of averaged ERS-2 SAR image with visual interpretation of GPR and IRE classification (Fig. 7). Fig. 7a, b present the Pauli decomposition product, where the combination of RGB colours is associated with scattering properties of different features. Comparison of Pauli decomposition with GPR visual interpretation and IRE classification shows that the green colour in Fig. 7a indicates well the ice and ice + in the ablation zone. White corresponds to equal amplitude over all polarimetric channels and offers a good presentation of the firn > 4.5 m zone. Due to the lack of GPR data we cannot characterise the violet colour properly, but it probably indicates firn < 4.5 m.

The results of the H-α Wishart classification (Fig. 7c) offer a very good example of discrimination between glacial zones. The only problem is a lack of differentiation between the ice and ice + zones. On the other hand, one additional class on the top of the ice cap (marked in yellow), not visible in the GPR interpretation, was identified. The extent of the additional zone is comparable to that of the shifted boundary between firn < 4.5 m and firn 4.5 > m of Fig. 6c. This indicates that this zone is firn with slightly different scattering properties in the volume, related to the natural continuity of the facies. It is worth

mentioning that the IRE classification corresponds closely with the extent of the groups of ice (ice and ice +) and firn (< 4.5 m and > 4.5 m) zones obtained via H-α segmentation (Fig. 7d). Only some of the IRE values defined as SI are not as clear as in the product of ALOS PALSAR segmentation; however, as in the previous analysis, this may be caused by the time window being fixed for the IRE calculations. H-α classification method, developed by Cloude and Pottier (1997), describes the scattering mechanism of each of the class, based on H-α plane. The description of each of the distinguished class proposed by Cloude and Pottier (1997) is provided in legends of Fig. 7c and d, however detailed analysis of this scheme are difficult to be obtained in this research, due to not sufficient amount of terrestrial data or comparable analysis from other glaciers on one hand, and high penetration of L-band and internal structures of the glacier on the other.

The results of k-means classification for the averaged ERS-2 SAR image (Fig. 7e) show, that as opposed to advanced polarimetric processing, it is possible to differentiate all glaciers facies, including the ice and the ice + zone. In contrast to the natural breaks classification of ERS-2 SAR sigma0, the SI zone was separated from that of firn < 4.5 m. Nevertheless, due to high amount of classes and remained noise, the results of k-means classification method are more difficult for their interpretation. Similarly, comparing IRE values and the results of the classification (Fig. 7f) is not as simple as in the case of H-α segmentation due to the high level of noise of IRE classification and high amount of classes at the k-means classification image. Nevertheless, the
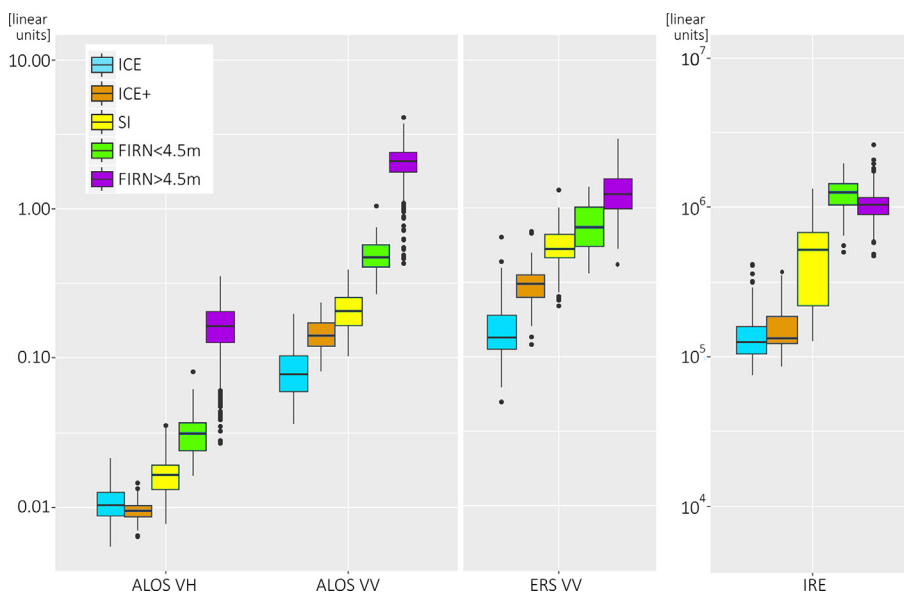

Fig. 5. Boxplots for distinguishing glacier facies based on ALOS PALSAR (left panel), averaged ERS-2 SAR (central panel) and IRE calculations (right panel) with classification based on visual interpretation. The solid horizontal lines represent median, the horizontal lines of boxes – first and third quartiles, the vertical lines (whiskers) – 1.5 interquartile range below the lower and above the upper quartiles, black dots – outliers. Note the y axes are in logarithmic scale.
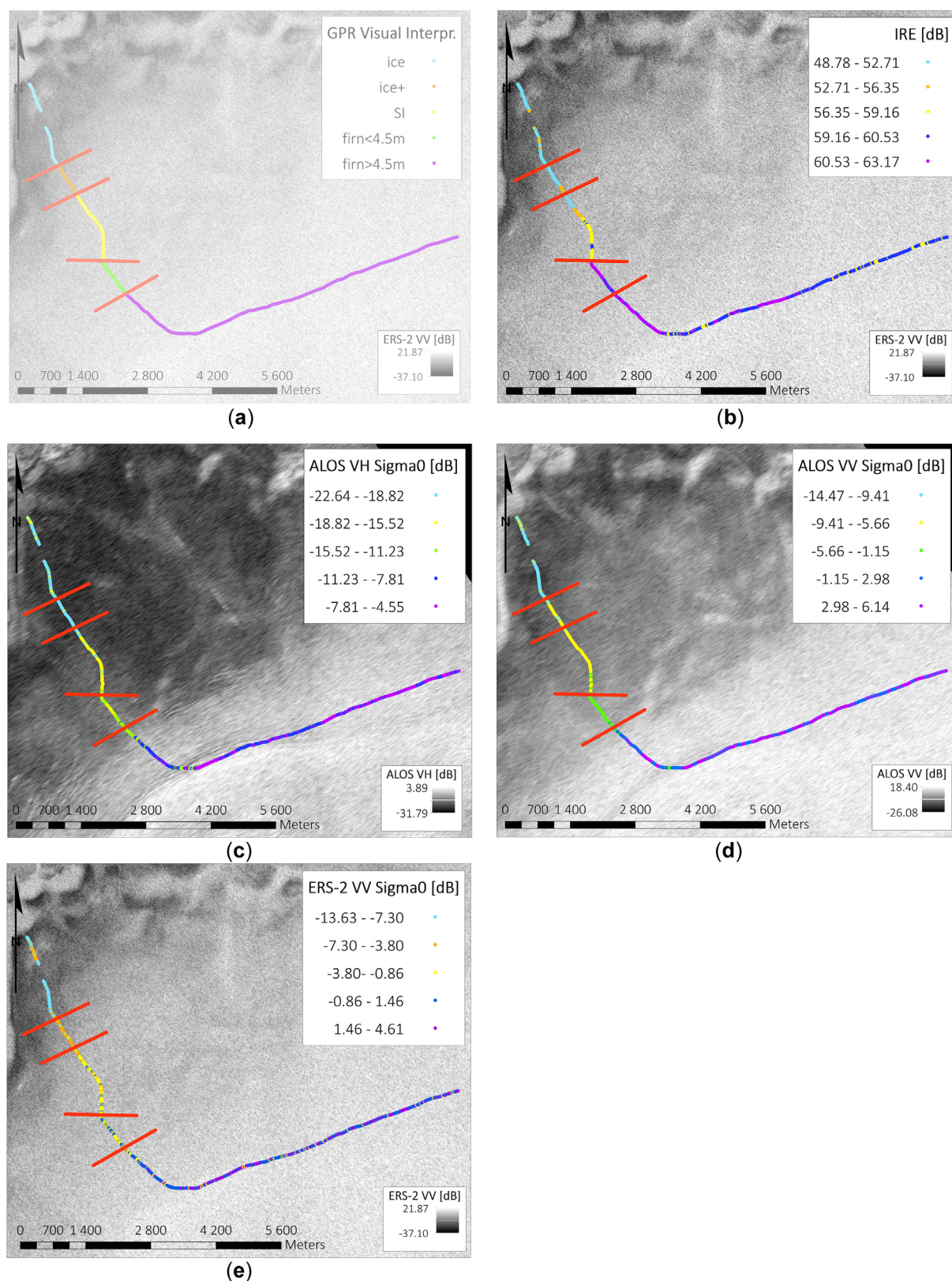
Fig. 6. Spatial distribution of: (a) results of GPR visual interpretation; (b) IRE; (c) sigma0 extraction for ALOS PALSAR VH polarisation; (d) sigma0 extraction for ALOS PALSAR VV polarisation; (e) sigma0 extraction for the averaged ERS-2 SAR image. For Figure a, b and e ERS-2 was used as a background; for c and d, ALOS PALSAR was used with VV and VH polarisation, respectively. Figures b, c, d and e present values classified by natural breaks (Jenks) classification method. Red lines represent boundaries between glaciers zones obtained from visual interpretation. (For interpretation of the references to colour in this figure legend, the reader is referred to the web version of this article.)

(a)

(b)

(c)

(d)

(e)

(f)
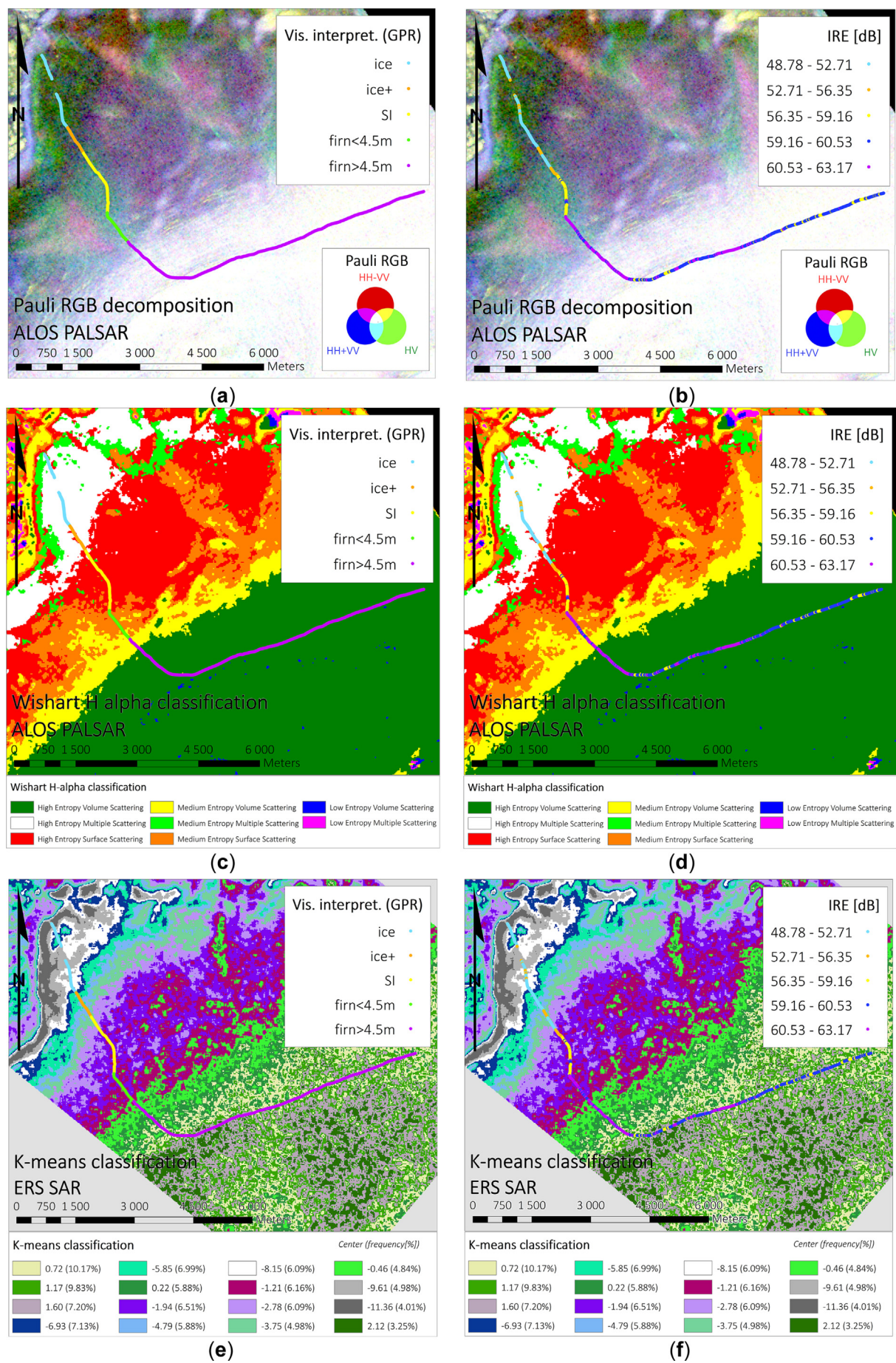
(caption on next page)

Fig. 7. Results of polarimetric analysis: Pauli RGB decomposition (a, b), H-α Wishart classification (c, d) (from Błaszczyk (2012), modified) and K-means classification of averaged ERS-2 SAR image (e, f) with GPR visual interpretation and IRE, respectively. The legends of H-α Wishart classification (c, d) is based on Cloude and Pottier (1997), classes of k-means classification (e, f) are described by the centres of each of the class and frequency of pixels (in brackets).

Table 3
Values of mean and standard deviation of IRE in each class (linear scale).

	Mean	Standard deviation
Ice	14.8×10^4	72.9×10^3
Ice+	16.3×10^4	71.0×10^3
SI	50.6×10^4	29.1×10^4
Firn $<$ 4.5 m	12.5×10^5	33.8×10^4
Firn $>$ 4.5 m	10.6×10^5	23.7×10^4

agreement between ice classes from both IRE and ERS-2 SAR image classification is noticeable.

6. Discussion

Due to the very remote location of Vestfonna and limitation of SAR satellites in this area at the end of accumulation season in 2008, when the in situ measurements were obtained, the study is limited to only several SAR images. Nevertheless, this is a next – important – step in the glaciers facies monitoring and the results present a high potential of applied methods in distinguishing glaciers facies.

The combination of GPR and SAR analysis for discrimination of glacier facies yields very promising results. Both sensors are sensitive to the character of the scatterers and thus are able to record the extent of glacier facies. Table 5 contains information about the potential for distinguishing glacier facies using the sensors differentiated according to the methods used in this study.

For natural breaks classification it is worth noting that ALOS PALSAR images, unlike averaged ERS-2 SAR, do not provide information about differences between the ice and ice+ zones (VH polarisation) or between the ice+ and SI (VV polarisation) zones. This is due to the difference in the wavelengths of the L- and C-bands, whereby the former penetrates more deeply. Therefore, such zones as firn $<$ 4.5 m and firn $>$ 4.5 m can be more easily distinguished.

The polarisation of the wave results in different capacities for distinguishing glacier facies. As the SAR images were obtained during dry, cold conditions, the C-band of the ERS-2 SAR sensor was capable of penetrating through a dry snow layer of at least 5 m depth (Rott et al., 1993; Hamran et al., 1997). This is in agreement with the results of the natural breaks classification of ERS-2 SAR sigma0, where firn $>$ 4.5 m was correctly classified. However, the boundary between SI and firn $<$ 4.5 m was not distinguished probably due to the limitations of the VV polarisation. The results of averaged ERS-2 SAR k-means classification indicate the possibility of distinguishing all zones. However, the high amount of classes makes the classification results difficult to interpret, therefore in situ data are especially needed. It is not recommended to perform glaciers facies analysis based only on one ERS-2 SAR image as the backscatter coefficient differs on separate images obtained during one month, even though dry snow conditions were preserved. Therefore, approach proposed by Langley et al. (2008) -

combining and averaging the SAR images is highly recommended, with at least five images in stock and a careful validation with in situ data analysis results. The lack of cross-polarised ERS-2 SAR imagery precludes performing further investigations, such as the segmentation algorithm proposed by Akbari et al. (2014). Natural breaks classification of the co-polarised ALOS PALSAR image does not provide information about the boundary between the ice+ and SI zones, which is also the boundary between the ablation and accumulation zones. Thus, for differentiation of these two zones, processing of either an averaged ERS-2 SAR or a cross-polarised ALOS PALSAR image is recommended.

As an alternative to time-consuming and subjective visual interpretation of GPR data for the purposes of validation of SAR data classification, we found that the IRE coefficient yields very promising results. Although not all glacier facies can be distinguished by IRE analysis, the most important ones, i.e. ice with ice+, SI, and firn, are indeed distinguishable. The only problem is that the extent of the SI zone for IRE classifications is smaller than that resulting from visual interpretation. This is likely due either to a fixed time window in the IRE calculations, so that part of the SI zone is not taken into account by IRE, or to the uncertainty of visual interpretation. The former can be eliminated in the future by applying a moving time window depending on the thickness of snow. The latter can be eliminated by using ground-truth data such as ice cores or snow pits along the GPR profile, as was done near Ahlmann Summit in 2009 (Beaudon et al., 2011; Möller et al., 2011a), but not along the GPR measurements. These data confirm the correct identification of the firn $>$ 4.5 m class.

Values of the IRE coefficient are also comparable to the results of H-α segmentation, in which all classes except ice and ice+ were distinguished. As in all analysis concerning IRE, a small part of the SI zone from IRE did not overlap with the segmentation results, again probably due to the fixed time window used in the IRE calculations. However, this polarimetric method yields very good results, with homogeneous classes, which correspond very well to the results of visual interpretation and IRE classification. If information about the extent of glacier ice is needed, k-means classification of ERS-2 SAR images offers a good solution. Despite the high noise level of the classified image, it is possible to distinguish all classes. However, validation of the k-means classification should be based on the visual interpretation method rather than on the IRE coefficient, due to the high noise of IRE and high amount of classes on processed SAR image.

7. Conclusions

In this study, several methods of classifying glacier zones were presented, using data from both SAR and GPR measurements. A novel approach – the Internal Reflection Energy (IRE) coefficient calculated from GPR data – was applied as a validation method for remote sensing analysis. The main findings from this study are as follows:

- The simplicity of the IRE calculation and its independence from the

Table 4
Mean and standard deviation of backscattering coefficients of ALOS PALSAR (VV and VH polarisation) and averaged ERS-2 SAR (VV) data in each class (linear scale).

	ALOS PALSAR (VH)		ALOS PALSAR (VV)		ERS-2 (VV)	
	Mean	Standard deviation	Mean	Standard deviation	Mean	Standard deviation
Ice	1.09×10^2	3.02×10^3	8.46×10^2	3.33×10^2	1.62×10^1	8.64×10^2
Ice+	9.56×10^3	1.58×10^3	1.46×10^1	3.74×10^2	3.20×10^1	1.18×10^1
SI	1.67×10^2	5.76×10^3	2.12×10^1	5.67×10^2	5.79×10^1	1.90×10^1
Firn $<$ 4.5 m	3.22×10^2	1.14×10^2	4.94×10^1	1.35×10^1	8.01×10^1	2.83×10^1
Firn $>$ 4.5 m	1.66×10^1	6.01×10^2	2.08	5.66×10^1	1.32	4.57×10^1

Table 5
Capacities of different sensors for distinguishing boundaries between glacier facies with differentiation of the methods used in this study.

Method	Data source	Ice/ice+	Ice+/SI	SI/firn < 4.5 m	Firn < 4.5 m/ firn > 4.5 m
Natural breaks classification	IRE (GPR)		✓	✓	
	ALOS VH		✓	✓	✓
	ALOS VV	✓		✓	✓
	ERS-2 VV	✓	✓		✓
H-α Wishart classification	ALOS PALSAR		✓	✓	✓
K-means classification	ERS-2	✓	✓	✓	✓

operator's degree of experience makes the coefficient a good tool for validation of SAR glacier facies analysis. IRE corresponds very closely to the ice (ice and ice+), SI and firn (< 4.5 m and > 4.5 m), albeit with a shifted boundary between ice+ and SI. This is probably due to the fixed time window of IRE calculation.

- Fully polarimetric ALOS PALSAR images enable more advanced processing methods to be performed, such as Pauli decomposition and H-α segmentation. In particular, the latter, yields very good results, corresponding very well to both visual interpretation and IRE classifications.
- The simple k-means classification of averaged ERS-2 SAR data provides information about the extent of all glacier facies. However, in situ data are especially needed for its interpretation and analysis based on several ERS-2 SAR images is recommended.
- ERS-2 SAR (C-band) is suited for distinguishing glacier facies in the lower part of the glacier, whereas ALOS PALSAR (L-band) imaging is recommended for the differentiation of SI and firn classes.
- Cross-polarised images (VH, HV) are more applicable for analysing glacier facies than co-polarised images (VV, HH).

In conclusion, the results of the study show that glacier facies – among them SI – can be distinguished by SAR analysis, including the simple k-means classification. However, especially good results were yielded by H-α Wishart classification, therefore, we would like to recommend this method for future glaciers facies detection. In addition, the IRE coefficient is recommended to be applied instead of the GPR visual interpretation method for the validation of remote sensing analysis. In the future – to avoid errors due to the fixed time window of the IRE calculation – the variation in the spatial distribution of snow cover should be taken into account. Ground-truth data such as shallow ice cores would be also valuable to add. All presented methods are recommended for accumulation season when dry snow conditions preserve extend of glacier facies from the end of the antecedent ablation season.

Author contributions

Barbara Barzycka, Małgorzata Błaszczyk, Mariusz Grabiec and Jacek Jania conceived and designed the experiments; Barbara Barzycka calculated, analysed and classified IRE and sigma0 coefficients, performed k-means classification and wrote the paper with the contribution of the co-authors. Małgorzata Błaszczyk provided SAR data and performed polarimetric analysis; Mariusz Grabiec provided the GPR data and made visual interpretation. The manuscript was commented on and edited by Małgorzata Błaszczyk, Mariusz Grabiec and Jacek Jania.

Conflicts of interest

The authors declare no conflict of interest.

Acknowledgements

References

Akbari, V., Doulgeris, A.P., Eltoft, T., 2014. Monitoring glacier changes using multi-temporal multipolarization SAR images. IEEE Trans. Geosci. Remote Sens. 52 (6), 3729–3741. https://doi.org/10.1109/TGRS.2013.2275203.

Baird, P.D., 1952. Part I: method of nourishment of the Barnes ice cap. J. Glaciol. 2 (11), 2–9. https://doi.org/10.3189/S0022143000025910.

Beaudon, E., Arppe, L., Jonsell, U., Martma, T., Möller, M., Pohjola, V.A., Scherer, D., Moore, J.C., 2011. Spatial and temporal variability of net accumulation from shallow cores from Vestfonna ice cap (Nordaustlandet, Svalbard). Geogr. Ann. Ser. B 93 (4), 287–299. https://doi.org/10.1111/j.1468-0459.2011.00439.x.

Benn, D., Evans, D.J.A., 2010. Glaciers and Glaciation, Second edition. Hodder Education, London978 0 340 905791.

Benson, C.S., 1961. Stratigraphic studies in the snow and firn of the Greenland ice sheet. Folia Geogr. Dan. 9, 13–37.

Błaszczyk, M., 2012. Porównanie Możliwości Identyfikacji Stref Lodowców na Podstawie Obrazów Radarowych ERS SAR Oraz ALOS PALSAR (Capability of glacier zone detection using radar images - ERS SAR and ALOS PALSAR). 24. Archiwum Fotogrametrii, Kartografii i Teledetekcji, pp. 21–30.

Brandt, O., Kohler, J., Lüthje, M., 2008. Spatial mapping of multi-year superimposed ice on the glacier Kongsvegen, Svalbard. J. Glaciol. 54 (184), 73–80. https://doi.org/10.3189/002214308784409080.

Braun, M.H., Schuler, T.V., Hock, R., Brown, I., Jackson, M., 2007. Comparison of remote sensing derived glacier facies maps with distributed mass balance modelling at Engabreen, northern Norway. IAHS Publ. 318, 126–134.

Brown, I.A., 2013. Multi-Temporal PolSAR Back Scatter Decomposition Over Glacier Ice, Snow and Firn. Vol. 722. ESA Living Planet Symposium, Edinburgh, United Kingdom, pp. 117.

Brown, I.A., Kirkbride, M.P., Vaughan, R.A., 1999. Find the firn line! The suitability of ERS-1 and ERS-2 SAR data for the analysis of glacier facies on Icelandic icecaps. Int. J. Remote Sens. 20 (15–16), 3217–3230. https://doi.org/10.1080/014311699211714.

Casey, J.A., Kelly, R.E.J., 2010. Estimating the equilibrium line of Devon Ice Cap, Nunavut, from RADARSAT-1 ScanSAR wide imagery. Can. J. Remote. Sens. 36 (S1), S41–S55. https://doi.org/10.5589/m10-013.

Cloude, S.R., Pottier, E., 1996. A review of target decomposition theorems in radar polarimetry. IEEE Trans. Geosci. Remote Sens. 34 (2), 498–518. https://doi.org/10.1109/36.485127.

Cloude, S.R., Pottier, E., 1997. An entropy based classification scheme for land applications of polarimetric SAR. IEEE Trans. Geosci. Remote Sens. 35 (1), 68–78. https://doi.org/10.1109/36.551935.

Cogley, J.G., 2009. Geodetic and direct mass-balance measurements: comparison and joint analysis. Ann. Glaciol. 50 (50), 96–100. https://doi.org/10.3189/172756409787769744.

Cogley, J.G., Hock, R., Rasmussen, L.A., Arendt, A.A., Bauder, A., Braithwaite, R.J., Jansson, P., Kaser, G., Möller, M., Nicholson, L., Zemp, M., 2011. Glossary of Glacier Mass Balance and Related Terms, IHP-VII Technical Documents in Hydrology No. 86, IACS Contribution No. 2. UNESCO-IHP, Paris.

De Smith, M.J., Goodchild, M.F., Longley, P., 2007. Geospatial Analysis: A Comprehensive Guide to Principles, Techniques and Software Tools. Troubador Publishing Ltd.https://doi.org/10.1111/j.1467-9671.2008.01122.x.

Doulgeris, A.P., Anfinsen, S.N., Larsen, Y., Langley, K., Eltoft, T., 2009. Evaluation of Polarimetric Configurations for Glacier Classification. International POLinSAR Workshop (POLinSAR2009), Frascati, Italy (January 26–30 2009).

Engeset, R.V., Kohler, J., Melvold, K., Lundén, B., 2002. Change detection and monitoring of glacier mass balance and facies using ERS SAR winter images over Svalbard. Int. J. Remote Sens. 23 (10), 2023–2050. https://doi.org/10.1080/01431160110075550.

Fahnestock, M., Bindschadler, R., Kwok, R., Jezek, K., 1993. Greenland ice sheet surface properties and ice dynamics from ERS-1 SAR imagery. Science 262 (5139), 1530–1534. https://doi.org/10.1126/science.262.5139.1530.

Ferretti, A., Monti, G.A., Prati, C., Rocca, F., Massonnet, D., 2007. InSAR Principles: Guidelines for SAR Interferometry Processing and Interpretation (TM-19, February 2007). ESA Publications, ESTEC, Postbus 299, 2200 AG Noordwijk, the Netherlands.

Gades, A.M., Raymond, C.F., Conway, H., Jacobel, R.W., 2000. Bed properties of Siple Dome and adjacent ice streams, West Antarctica, inferred from radio-echo sounding measurements. J. Glaciol. 46 (152), 88–94. https://doi.org/10.3189/172756500781833467.

Grabiec, M., 2017. Stan i Współczesne Zmiany Systemów Lodowcowych Południowego Spitsbergenu w Świetle Badań Metodami Radarowymi (The state and contemporary changes of glacial systems in southern Spitsbergen in the light of radar methods). Wydawnictwo Uniwersytetu Śląskiego, Katowice (ISBN-13: 978-83-226-3015-0).

Grabiec, M., Puczko, D., Budzik, T., Gajek, G., 2011. Snow distribution patterns on Svalbard glaciers derived from radio-echo soundings. Polish Polar Res. 32 (4), 393–421. https://doi.org/10.2478/v10183-011-0026-4.

Gusmeroli, A., Wolken, G.J., Arendt, A.A., 2014. Helicopter-borne radar imaging of snow cover on and around glaciers in Alaska. Ann. Glaciol. 55 (67), 78–88. https://doi.org/10.3189/2014AoG67A029.

Hall, D.K., 1996. Remote sensing applications to hydrology; imaging radar. Hydrol. Sci. J. 41 (4), 609–624. https://doi.org/10.1080/02626669609491528.

Hall, D.K., Kelly, R.E., Foster, J.L., Chang, A.T., 2005. Estimation of snow extent and snow properties. In: Anderson, M.G., McDonnell, J.J. (Eds.), Encyclopedia of Hydrological Sciences. John Wiley & Sons, 9780470848944, pp. 813–829. https://doi.org/10.1002/0470848944.hsa062.

Hamran, S.E., Guneriussen, T., Hagen, J.O., Odegard, R., 1997. Ground penetration radar and ERS SAR data for glacier monitoring. In: Geoscience and Remote Sensing, 1997. Vol. 2. IGARSS '97. Remote Sensing - A Scientific Vision for Sustainable Development., 1997 IEEE International, pp. 634–636. (vol.632). https://doi.org/10.1109/IGARSS.1997.615207.

Huang, L., Li, Z., Tian, B.S., Chen, Q., Liu, J.L., Zhang, R., 2011. Classification and snow line detection for glacial areas using the polarimetric SAR image. Remote Sens. Environ. 115 (7), 1721–1732. https://doi.org/10.1016/j.rse.2011.03.004.

Huang, L., Li, Z., Tian, B.-s., Chen, Q., Zhou, J.-m., 2013. Monitoring glacier zones and snow/firn line changes in the Qinghai–Tibetan Plateau using C-band SAR imagery. Remote Sens. Environ. 137, 17–30. https://doi.org/10.1016/j.rse.2013.05.016.

Jaenicke, J., Mayer, C., Scharrer, K., Münzer, U., Gudmundsson, Á., 2006. The use of remote-sensing data for mass-balance studies at Mýrdalsjökull ice cap, Iceland. J. Glaciol. 52 (179), 565–573. https://doi.org/10.3189/172756506781828340.

Jania, J., Macheret, Y.Y., Navarro, F.J., Glazovsky, A.F., Vasilenko, E.V., Lapazaran, J., Glowacki, P., Migala, K., Balut, A., Piwowar, B.A., 2005. Temporal changes in the radiophysical properties of a polythermal glacier in Spitsbergen. Ann. Glaciol. 42 (1), 125–134. https://doi.org/10.3189/172756405781812754.

Jenks, G.F., Caspall, F.C., 1971. Error on choroplethic maps: definition, measurement, reduction. Ann. Assoc. Am. Geogr. 61 (2), 217–244. https://doi.org/10.1111/j.1467-8306.1971.tb00779.x.

Kanagaratnam, P., Gogineni, S.P., Pamasami, V., Braaten, D., 2004. A wideband radar for high-resolution mapping of near-surface internal layers in glacial ice. IEEE Trans. Geosci. Remote Sens. 42 (3), 483–490. https://doi.org/10.1109/TGRS.2004.823451.

König, M., Winther, J.G., Knudsen, N.T., Guneriussen, T., 2000, June. Equilibrium-and firn-line detection with multi-polarization SAR–first results. In: Proc. Workshop EARSeL-Special Interest Group 'Land Ice and Snow'.

König, M., Winther, J.G., Isaksson, E., 2001a. Measuring snow and glacier ice properties from satellite. Rev. Geophys. 39 (1), 1–27. https://doi.org/10.1029/1999RG000076.

König, M., Winther, J.G., Knudsen, N.T., Guneriussen, T., 2001b. Firn-line detection on Austre Okstindbreen, Norway, with airborne multipolarization SAR. J. Glaciol. 47 (157), 251–257. https://doi.org/10.3189/172756501781832241.

König, M., Wadham, J., Winther, J.G., Kohler, J., Nuttall, A.M., 2002. Detection of su-perimposed ice on the glaciers Kongsvegen and midre Lovenbreen, Svalbard, using SAR satellite imagery. Ann. Glaciol. 34 (1), 335–342. https://doi.org/10.3189/172756402781817617.

König, M., Winther, J.G., Kohler, J., König, F., 2004. Two methods for firn-area and mass-balance monitoring of Svalbard glaciers with SAR satellite images. J. Glaciol. 50 (168), 116–128. https://doi.org/10.3189/172756504781830286.

Langley, K., Hamran, S.E., Hogda, K.A., Storvold, R., Brandt, O., Kohler, J., Hagen, J.O., 2008. From glacier facies to SAR backscatter zones via GPR. IEEE Trans. Geosci. Remote Sens. 46 (9), 2506–2516. https://doi.org/10.1109/TGRS.2008.918648.

Laur, H., Bally, B., Meadows, P., Sanchez, J., Schaettler, B., Lopinto, E., Esteban, D., 2004. ERS SAR Calibration: Derivation of o⁰ in ESA ERS SAR PRI Products. Tech. rep., Document no.: ES-TN-RS-PM-HL09, Issue 2, Rev. 5f., 5. November. European Space Agency (ESA).

Lavalle, M., Wright, T., 2009. Absolute Radiometric and Polarimetric Calibration of ALOS PALSAR Products Generated Within ADEN, Document Issue (1), Revision (3), 19/05/2009.

Lee, J.S., Grunes, M.R., Kwok, R., 1994. Classification of multi-look polarimetric SAR imagery based on complex Wishart distribution. Int. J. Remote Sens. 15 (11), 2299–2311. https://doi.org/10.1080/01431169408954244.

Lee, J.S., Grunes, M.R., Ainsworth, T.L., Li-Jen, D., Schuler, D.L., Cloude, S.R., 1999. Unsupervised classification using polarimetric decomposition and the complex Wishart classifier. IEEE Trans. Geosci. Remote Sens. 37 (5), 2249–2258. https://doi.org/10.1109/36.789621.

Lillesand, T., Kiefer, R.W., Chipman, J., 2008. Microwave and LIDAR sensing. In: Remote Sensing and Image Interpretation, 6th edition. John Wiley & Sons, 978-0-470-05245-7, pp. 626–726.

López-Martínez, C., Ferro-Famil, L., Pottier, E., 2005. PolSARpro v4.0 Polarimetry Tutorial. URL. http://earth.esa.int/polsarpro/tutorial.htmlEuropean Space Agency, Paris, France.

MacQueen, J., 1967. Some methods for classification and analysis of multivariate ob-servations. In: Proceedings of the Fifth Berkeley Symposium on Mathematical Statistics and Probability, Volume 1: Statistics. No. 14. University of California Press, Berkeley, Calif., pp. 281–297.

Massom, R., Lubin, D., 2006. Polar Remote Sensing: Volume II: Ice Sheets. Springer-Verlag, Berlin Heidelberg3-540-26101-X.

Melvold, K., Hauck, Ch., Kneisel, Ch., 2008. Snow measurements using GPR: example from Amundsenisen, Svalbard. In: Applied Geophysics in Periglacial Environments. Cambridge University Press, Cambridge, pp. 207–216.

Möller, M., Finkelnburg, R., Braun, M., Hock, R., Jonsell, U., Pohjola, V.A., Scherer, D., Schneider, C., 2011a. Climatic mass balance of the ice cap Vestfonna, Svalbard: a spatially distributed assessment using ERA-interim and MODIS data. J. Geophys. Res. Earth Surf. 116 (F3). https://doi.org/10.1029/2010JF001905.

Möller, M., Möller, R., Beaudon, É., Mattila, O.P., Finkelnburg, R., Braun, M., Grabiec, M., Jonsell, U., Luks, B., Puczko, D., 2011b. Snowpack characteristics of Vestfonna and De Geerfonna (Nordaustlandet, Svalbard) – a spatiotemporal analysis based on multiyear snow-pit data. Geogr. Ann. Ser. B 93 (4), 273–285. https://doi.org/10.1111/j.1468-0459.2011.00440.x.

Müller, F., 1962. Zonation in the accumulation area of the glaciers of Axel Heiberg Island, N.W.T., Canada. J. Glaciol. 4 (33), 302–311. https://doi.org/10.1017/S0022143000027623.

Navarro, F.J., Macheret, Y.Y., Benjumea, B., 2005. Application of radar and seismic methods for the investigation of temperate glaciers. J. Appl. Geophys. 57 (3), 193–211. https://doi.org/10.1016/j.jappgeo.2004.11.002.

Nuth, C., Moholdt, G., Kohler, J., Hagen, J.O., Kääb, A.C.F., 2010. Svalbard glacier ele-vation changes and contribution to sea level rise. J. Geophys. Res. Earth Surf. 115 (F1). https://doi.org/10.1029/2008JF001223.

Obleitner, F., Lehning, M., 2004. Measurement and simulation of snow and superimposed ice at the Kongsvegen glacier, Svalbard (Spitzbergen). J. Geophys. Res.-Atmos. 109 (D4). https://doi.org/10.1029/2003JD003945.

Partington, K.C., 1998. Discrimination of glacier facies using multi-temporal SAR data. J. Glaciol. 44 (146), 41–53. https://doi.org/10.1017/S0022143000000422.

Rees, W.G., 2005. Remote Sensing of Snow and Ice. CRC Press978-0-415-29831-5.

Rignot, E., Echelmeyer, K., Krabill, W., 2001. Penetration depth of interferometric syn-thetic-aperture radar signals in snow and ice. Geophys. Res. Lett. 28 (18), 3501–3504. https://doi.org/10.1029/2000GL012484.

Rott, H., Mätzler, C., 1987. Possibilities and limits of synthetic aperture radar for snow and glacier surveying. Ann. Glaciol. 9 (1), 195–199. https://doi.org/10.1017/S0260305500000604.

Rott, H., Nagler, T., 1993. Snow and glacier investigations by ERS-1 SAR: first results. In: Proceedings of the First ERS-1 Symposium—Space at the Service of Our Environment, ESA SP-359. ESTEC Publishing Division, Cannes, France, pp. 577–583.

Rott, H., Sturm, K., Miller, H., 1993. Active and passive microwave signatures of Antarctic firn by means of field measurements and satellite data. Ann. Glaciol. 17 (1), 337–343. https://doi.org/10.1017/S0260305500013070.

Sauter, T., Möller, M., Finkelnburg, R., Grabiec, M., Scherer, D., Schneider, C., 2013. Snowdrift modelling for the Vestfonna ice cap, north-eastern Svalbard. Cryosphere 7 (4), 1287–1301. https://doi.org/10.5194/tc-7-1287-2013.

Schwarz, Gideon E., 1978. Estimating the dimension of a model. Ann. Stat. 6 (2), 461–464. https://doi.org/10.1214/aos/1176344136.

Singh, G., Yamaguchi, Y., Park, S.E., Venkataraman, G., 2010. Identification of snow using SAR polarimetry techniques. In: International Archives of the Photogrammetry, Remote Sensing and Spatial Information Science. ISPRS, Kyoto, Japan, pp. 146–149.

Singh, G., Venkataraman, G., Yamaguchi, Y., Park, S.E., 2014. Capability assessment of fully polarimetric ALOS–PALSAR data for discriminating wet snow from other scat-tering types in mountainous regions. IEEE Trans. Geosci. Remote Sens. 52 (2), 1177–1196. https://doi.org/10.1109/TGRS.2013.2248369.

Small, D., Schubert, A., 2008. Guide to ASAR Geocoding. 1 RLS, University of Zurich.

SNAP ESA, 2018. SNAP - ESA Sentinel Application Platform. European Space Agency. http://step.esa.int, Version 6.0.3.

Tebaldini, S., Nagler, T., Rott, H., Heilig, A., 2016. Imaging the internal structure of an alpine glacier via L-band airborne SAR tomography. IEEE Trans. Geosci. Remote Sens. 54 (12), 7197–7209. https://doi.org/10.1109/TGRS.2016.2597361.

Thorndike, R.L., 1953. Who belongs in the family? Psychometrika 18 (4), 267–276. https://doi.org/10.1007/BF02289263.

Venkataraman, G., Singh, G., Rao, Y.S., 2007. Snow cover monitoring and snow density estimation using ALOS-PALSAR data. In: Proceedings of First PI Symposium. Kyoto, Japan.

Wakahama, G., Kuroiwa, D., Hasemi, T., Benson, C.S., 1976. Field observations and ex-perimental and theoretical studies on the superimposed ice of McCall Glacier, Alaska. J. Glaciol. 16 (74), 135–149. https://doi.org/10.1017/S0022143000031488.

Wright, A., Wadham, J., Siegert, M., Luckman, A., Kohler, J., 2005. Modelling the impact of superimposed ice on the mass balance of an Arctic glacier under scenarios of future climate change. Ann. Glaciol. 42 (1), 277–283. https://doi.org/10.3189/172756405781813104.

Zemp, M., Hoelzle, M., Haeberli, W., 2009. Six decades of glacier mass-balance ob-servations: a review of the worldwide monitoring network. Ann. Glaciol. 50 (50), 101–111. https://doi.org/10.3189/172756409787769591.